Multivariable-Modulation-Based Conduction Loss Minimization in a Triple-Active-Bridge Converter

Saikat Dey, *Student Member, IEEE*, and Ayan Mallik, *Member, IEEE*

***Abstract*—This article presents the design, development, and optimization of pulsewidth modulation (PWM) scheme of an isolated bidirectional triple-active-bridge (TAB) dc–dc converter composed of three full-bridge modules and a high-frequency planar transformer. This article aims at improving the efficiency of the TAB converter by means of conduction loss minimization. The approach utilizes multiple control variables as degrees of freedom for the converter modulation. The optimization is based on the minimization of the true rms current, formulated using generalized harmonic approximation technique. The approach constitutes of two steps: the modulation pattern with least algorithmic complexity for efficiency maximization is first found depending on the operating load and gain condition, and, subsequently, the optimum control variables are calculated using the gradient descent algorithm applied on the identified modulation pattern. An 800-W TAB converter proof-of-concept is built to verify all theoretical considerations and model-oriented analysis. While the converter has an input dc bus voltage of 160 V, the two output ports of the converter can deliver 400 W each at voltage levels of 110–130 V and 18–27 V, respectively. With the implementation of the proposed optimal phase-duty control, the experimental results show a nonunity gain light load efficiency increment up to 6.1% compared with the conventional modulation technique.**

***Index Terms*—Bidirectional power flow, dc–dc power converters, pulse width modulation converters.**

I. Introduction

HIGH penetration of renewable energy sources and storage in recent times has drawn attention toward multiport converters (MPC) as a potential solution for versatile energy management systems [1]. The MPCs can integrate multiple sources, storages, and loads with varied voltage and current ratings into a single power stage allowing multidirectional power flow between its ports with applications in electric vehicles [2] to more-electric aircraft [3]. One of the promising topologies in the multiwinding transformer-coupled MPC family is the triple-active-bridge (TAB) converter, which is a multiport network with three full bridges connected via a high-frequency multiwinding transformer [4], [5]. Derived from the dual-active-bridge (DAB) converter family [6], [7], the TAB converter integrates and exchanges the energy from/to all ports, provides full isolation among all ports, and can match the different port voltage levels.

The basic TAB modulation (dual phase shift or DPS) uses 50% duty cycles on all three full bridges and uses the phase shifts between the full-bridge cell voltages to transfer power between the ports [8]. However, DPS technique with only phase control leads to high transformer winding currents and hence higher conduction losses under light-load conditions and nonunity voltage gains with mismatches in the port voltages, which thus calls for an improved multivariable-based modulation scheme minimizing the system conduction losses. More general modulation techniques are possible by using different modulation patterns for the three bridges. For example, the control of each port's duty cycle ratio, besides its phase shift, is also possible at the cost of additional computational complexity and difficulty in implementation.

The basic concept of efficiency improvements in the TAB converter in terms of conduction loss utilizing the duty cycle control variables originates from the existing efficiency optimization techniques for the DAB dc–dc converter [9]–[13]. Yet, from the DAB to the TAB, there is a significant gap in terms of circuit analysis and computational efforts. Since one more port is added, the transformer's input current expressions include three more variables, i.e., the port voltage, duty cycle, and phase-shift angle. Moreover, adding the third port is not an extension of a DAB in terms of the mathematical formulation of transformer's winding current expressions. Since the third port is highly coupled with the initial two ports, the transformer's current expressions including the power flow criteria of even the initial two ports are entirely modified in a TAB. Thus, the optimal phase-duty control-based loss optimization of a TAB is difficult to achieve from the time-domain-based DAB analysis knowledge base and is rarely found in the literature [14].

The scope of efficiency improvements by applying higher order modulation schemes in the MPC dc–dc converters is identified by the work presented [8], [14]–[26]. However, most of these research efforts involve complex time-domain-based multimode-switching-based control strategies. Also, none of these research works result in a computationally efficient and generic five-variable converter control strategy that optimizes the overall conduction loss in the TAB converter.

In [8], duty cycle and phase-shift modulation are introduced for achieving lower losses, on the basis of fundamental component analysis of the converter's voltages and currents. In [8], the concept of circulating power has been introduced, which,

Manuscript received September 28, 2021; revised November 30, 2021; accepted January 2, 2022. Date of publication January 7, 2022; date of current version February 18, 2022. This work was supported in part by CoolCAD Electronics, LLC. Recommended for publication by Associate Editor Y. Siwakoti. *(Corresponding author: Ayan Mallik.)*

The authors are with the Systems Engineering Department, Polytechnic School, Arizona State University, Mesa, AZ 85212 USA (e-mail: sdey27@asu.edu; ayan.mallik@asu.edu).

Color versions of one or more figures in this article are available at https://doi.org/10.1109/TPEL.2022.3141334.

Digital Object Identifier 10.1109/TPEL.2022.3141334

however, is not correlated with any kind of losses and hence not used in any specific type of loss optimization or efficiency maximization process. Although fundamental harmonic approximation (FHA) is effective at moderate-to-high power transfer among the ports, the true power loss differs from the estimated power loss at lighter load demand, which limits the performance attained by this approach [15]. Moreover, FHA misses most of the insights into the shape of the switching patterns that are critical to accurately correlate rms current levels with the phase/duty control variables.

Moreover, due to the higher number of degrees of freedom and superpositions of port voltages applied to a transformer, the TAB converters have several tens of operating modes. The complexity makes the use of time-domain-analysis-based rms current computation methods [15] that are computationally heavy and time-intensive. Furthermore, digital implementation of a time-domain-analysis-based pulsewidth modulation (PWM) control strategy is complicated since the current and voltage dynamics change in each switching pattern. The implementation becomes even more involved with an increasing number of switching patterns when the modulation changes from the basic DPS modulation to any higher order PWM techniques. On the contrary, this article presents a harmonic form bridge voltage expression utilizing the generalized harmonic approximation (GHA) model, which facilitates the synthesis of a unified interpretation of the transformer's current irrespective of the switching modulation pattern and number of control variables involved. It, therefore, makes expression more concise and eases down the digital control implementation.

Another challenging issue in the TAB converter is its efficiency degradation, particularly at lighter load and nonunity gain operation under DPS-based PWM control. A very few works have been carried out in the literature focusing on the light-load, wide gain efficiency optimization of the TAB dc–dc converter [8], [15]. However, no study has been performed to address the following challenges:

1) establishing accurately quantified relationship between the port/winding voltages, currents, power flow, and the control variables, such as φ_i and δ_j;
2) mathematical correlation of the major system loss with the phase/duty control variables;
3) the optimal choice of the phase/duty combination for ensuring minimum mean-square currents under any input/output voltage/power conditions;
4) identification of the most favorable TAB modulation technique depending on the operating gain and load condition.

This article puts forward a substantial effort to address all the above-mentioned hurdles by proposing a hybrid phase-duty control-based conduction loss minimization strategy in a dual-output triple-active-bridge (TAB) dc–dc converter. Here, the objective function for optimization is formulated considering conduction loss only because it majorly contributes to the total system loss at a nonunity gain and light-load operating point. In order to validate the contribution of this article, it is critical to evaluate the proposed modulation strategy with the existing DPS or any higher order control approaches mentioned in recent literature [8], [14]–[17]. Although in [14], an effort to identify the zero-voltage switching (ZVS) criterion in a TAB converter under DPS or TPS mode of operation is proposed, it does not provide a solution to optimize the system loss by applying a particular control strategy. The concept of a five-variable-based TAB control strategy is introduced in [15], which showcases the possibility of conduction loss reduction under wide-voltage-gain conditions. However, the implementation of this control logic becomes memory and computation intensive as the converter analysis is done in time domain with a large set of operating modes. Also, the application of penta-phase-shift (PPS)-based control for all the loading conditions limits the switching frequency of the converter by extending the execution time of the control logic. The existing challenges call for utilizing a computationally optimized and efficient multivariable control strategy, proposed in this article, that can minimize the overall system loss in a TAB dc–dc converter under all output voltage gain and loading conditions.

The converter in this study is designed to be rated for 400 W at each of the output ports, where the low-voltage-port dc bus has a battery voltage range from 18 to 26 V, and the high-voltage port can have a dc voltage ranging between 110 and 130 V, which are the standard voltage levels for NASA space shuttles [28]. The key contributions of this article can be summarized as follows:

1) unique converter architecture and control strategy to enable any directional desired power flow between all the ports connected in the system;
2) accurate quantification of the winding currents and the power flow between the ports by employing the frequency-domain GHA model representing the port bridge voltages;
3) multiple-control-variable-based switching modulation optimization technique in order to ensure the desired interport power flow while achieving minimum sum of mean-square currents in three ports;
4) adaptive identification of the most favorable modulation technique corresponding to the ports' voltage gain and load condition;
5) digital-domain implementation of the composite optimal PWM strategy in a TAB controller using the proposed gradient descent algorithm.

II. TAB Converter Operation, GHA-Based Modeling, and Power Transfer Criteria

Fig. 1 shows the schematic of the TAB converter, where V_1, V_2', and V_3' represent three dc voltage sources or loads connected to a three-terminal transformer via three full-bridge cells. The transformer acts as an ac-link that couples these ports at different voltage levels by its corresponding turn ratios, given as n_1:n_2:n_3. The inductors L_1, L_2', and L_3' can be inserted as separate components or can be formed using the transformer's leakage inductances. The phase shifts of the gate driving signals of the respective half-bridge switches of all the ports with respect to the reference half-bridge of the first port result in the full-bridge output voltages v_2' and v_3' (depicted in Fig. 2), phase displaced by $\varphi_2$and $\varphi_3$with respect to v_1. Along with the phase modulation, to incorporate duty cycle control of v_1, v_2', and v_3', two half-bridge control signals of the same full

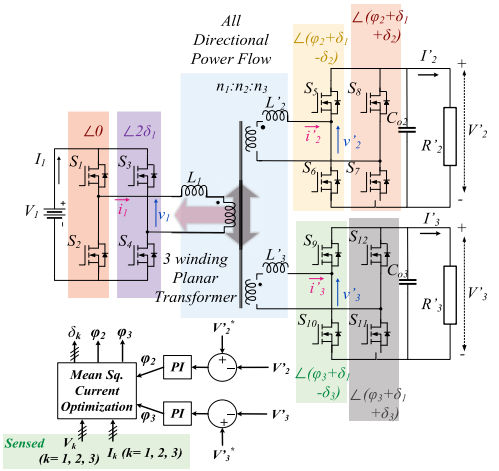

Fig. 1. TAB converter topology and phase shifts of the individual half-bridge gating signals.

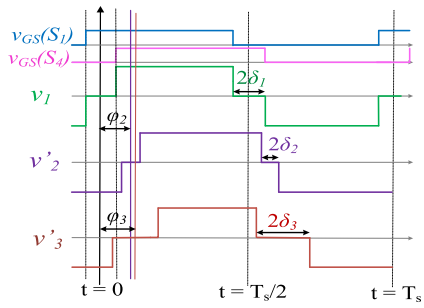

Fig. 2. Full-bridge output voltages in relation with the gate signal phase displacements of the individual half-bridges.

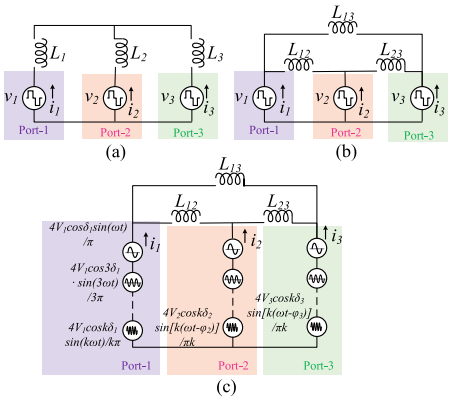

Fig. 3. (a) Y-equivalent and (b) Δ-equivalent circuit of TAB. (c) GHA-based modeling of the port voltages, approximated up to "*k*"th order.

bridges are phase displaced by $2\delta_1$, $2\delta_2$, and $2\delta_3$ amount. It is noteworthy that φ_2 and φ_3 range between $-\pi/2$ and $\pi/2$, whereas the range of $\delta_k (k = 1, 2 \text{ or } 3)$ falls between 0 and $\pi/2$. The simplified schematic of the TAB network is shown in Fig. 3(a) and (b) along with the transformation of the transformer and the inductor network from a Y-model into Δ-model. Throughout this article, the Δ-model (referenced to the primary side of the transformer) is used to analyze the operation of the TAB converter. Thus, the modified bridge voltage and currents are represented as follows: $i_2 = i_2' \left(\frac{n_2}{n_1}\right)$, $i_3 = i_3' \left(\frac{n_3}{n_1}\right)$; $v_2 = v_2' \left(\frac{n_1}{n_2}\right)$, $v_3 = v_3' \left(\frac{n_1}{n_3}\right)$ and $V_2 = V_2' \left(\frac{n_1}{n_2}\right)$, $V_3 = V_3' \left(\frac{n_1}{n_3}\right)$. As described in [7], the link inductances in the Δ-model can be computed from the individual leakage inductances of the transformer windings in the Y-model as $L_{12} = L_1 + L_2 + \frac{L_1 L_2}{L_3}$, $L_{13} = L_1 + L_3 + \frac{L_1 L_3}{L_2}$, and $L_{23} = L_2 + L_3 + \frac{L_2 L_3}{L_1}$, $L_2 = L_2' \left(\frac{n_1}{n_2}\right)^2$and $L_3 = L_3' \left(\frac{n_1}{n_3}\right)^2$.

In this circuit topology, the port or full-bridge cell voltages are of a quasi-square wave shape that can be decomposed in an infinite sum Fourier series. However, approximating the generalized harmonic model up to *n*th harmonic order, the ac port voltages can be presented as follows:

$$v_1\ (t) = \frac{4V_1}{\pi} \sum_{k=1}^{n=2m+1} \frac{1}{k} \cos(k\delta_1) \sin(k\omega t) \tag{1}$$

$$v_2\ (t) = \frac{4V_2}{\pi} \sum_{k=1}^{n=2m+1} \frac{1}{k} \cos(k\delta_2) \sin\{k(\omega t - \varphi_2)\} \tag{2}$$

$$v_3\ (t) = \frac{4V_3}{\pi} \sum_{k=1}^{n=2m+1} \frac{1}{k} \cos(k\delta_3) \sin\{k(\omega t - \varphi_3)\} \tag{3}$$

where "*k*" is the order of the harmonic, *m* is a positive integer, and $\omega = 2\pi f_{\text{sw}}$, with f_{sw} being the switching frequency of the converter. Thus, each port voltage can be expressed as a series combination of sinusoidal voltage sources of $kf_{\text{sw}}\ (k = 1, 3, 5, \ldots, 2m+1)$ frequency, as shown in Fig. 3(c).

The inductor currents, flowing between two ports, in the circuit described in delta convention can be calculated as, $i_{ab} = \int_0^t \frac{v_{ab}(t)dt}{L_{ab}} = \frac{1}{L_{ab}} \int_0^t v_{ab}(t)dt = \frac{1}{L_{ab}} \int_0^t [v_a(t) - v_b(t)]dt$, where, i_{ab} is the current flowing from port-a to port-b and v_{ab} is the voltage across the inductance L_{ab}. Now, using the relations given in (1)–(3), the primary winding transformer current in the delta equivalent circuit can be written as follows:

$$i_{12}\ (t) = \frac{4}{\pi\omega L_{12}} \sum_{k=1}^{2m+1} \left[-\frac{V_1}{k^2} \cos(k\delta_1) \cos(k\omega t) + \frac{V_2}{k^2} \cos(k\delta_2) \cos\{k(\omega t - \varphi_2)\} \right] \tag{4}$$

$$i_{13}\ (t) = \frac{4}{\pi\omega L_{13}} \sum_{k=1}^{2m+1} \left[-\frac{V_1}{k^2} \cos(k\delta_1) \cos(k\omega t) + \frac{V_3}{k^2} \cos(k\delta_3) \cos\{k(\omega t - \varphi_3)\} \right] \tag{5}$$

$$i_{23}\ (t) = \frac{4}{\pi\omega L_{23}} \sum_{k=1}^{2m+1} \left[-\frac{V_2}{k^2} \cos(k\delta_2) \cos\{k(\omega t - \varphi_2)\} + \frac{V_3}{k^2} \cos(k\delta_3) \cos\{k(\omega t - \varphi_3)\} \right]. \tag{6}$$

Applying Kelvin's circuit law (KCL) at the individual port nodes, the total current sourced by a port can be formulated as

follows:

$$i_1\ (t) = i_{12}\ (t) + i_{13}\,(t)\,. \tag{7}$$

Substituting (4) and (5) into (7), i_1 can be derived and simplified as follows:

$$i_1 = \sum_{k=1}^{2m+1} \left[A_{\rm k} \sin\left(k\omega t\right) + B_{\rm k}\cos\left(k\omega t\right)\right] \tag{8}$$

where the harmonic order "k"-dependent coefficients are $A_{\rm k} = \frac{4V_1}{\pi\omega k^2}\ [\frac{m_2\cos(k\delta_2)\sin(k\varphi_2)}{L_{12}} + \frac{m_3\cos(k\delta_3)\sin(k\varphi_3)}{L_{13}}]$ and $B_{\rm k} = \frac{4V_1}{\pi\omega k^2}\ [\frac{m_2\cos(k\delta_2)\cos(k\varphi_2)-\cos(k\delta_1)}{L_{12}} + \frac{m_3\cos(k\delta_3)\cos(k\varphi_3)\ -\cos(k\delta_1)}{L_{13}}]$; the individual port output voltage gains with respect to input port 1 are denoted as $m_2 = \frac{V_2}{V_1}$ and $m_3 = \frac{V_3}{V_1}$. Now, the port-1 current rms is determined as follows (9) shown at bottom of this page, where $d_{k1} = \cos(k\delta_1)$, $d_{k2} = \cos(k\delta_2)$, and $d_{k3} = \cos(k\delta_3)$. Similar to $i_{1,\rm RMS}$, utilizing the above-mentioned process, the rms currents flowing through the two output-side transformer windings, i_2' and i_3', can be also quantified and determined from (10) and (11), respectively shown at bottom of this page.

It is evident from (9)–(11) that the accuracy of the calculation of the port rms currents depends on the incorporation of switching harmonic order. Fig. 4 presents two test cases where the primary winding current shape is predicted as the superposition of different harmonic orders (n) for an operating control variable set given by $(\delta_1, \delta_2, \delta_3, \varphi_2, \varphi_3)$ = (case a) (0.8, 0.918, 0.656, 0.625, 0.257) and (case b) (0.38, 0.212, 0.462, 0.397, 0.124). The variations of the theoretically calculated rms current levels with the considered harmonic order and their comparison with the actual primary winding rms current from simulation are provided in Table I. It is evident from the data that using (9), the rms current can be predicted accurately for $n \geq 7$ with an error margin of less than 0.6%.

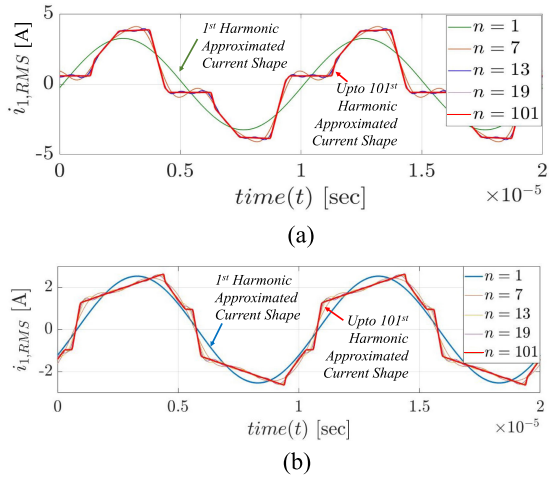

Fig. 4. Approximated i_1 current shape considering different orders of harmonics using the GHA model for $(\delta_1, \delta_2, \delta_3, \varphi_2, \varphi_3)$ = (a) (0.8, 0.918, 0.656, 0.625, 0.257) and (b) (0.38, 0.212, 0.462, 0.397, 0.124).

$$\begin{aligned} i_{1,\rm rms}^2 = \frac{1}{2}\sum_{k\,=\,1}^{2m+1}\frac{1}{k^4}\left[A_{\rm k}^2 + B_{\rm k}^2\right] \ &= \frac{8V_1^2}{\pi^2\omega^2}\cdot\sum_{k\,=\,1}^{2m+1}\frac{1}{k^4}\left[d_1^2\left(\frac{1}{L_{12}^2}+\frac{1}{L_{13}^2}+\frac{2}{L_{12}L_{13}}\right)\right. \\ &+ \frac{m_2^2d_2^2}{L_{12}^2}+\frac{m_3^2d_3^2}{L_{13}^2} - 2d_1d_2m_2\cos\left(k\varphi_2\right)\left(\frac{1}{L_{12}^2}+\frac{1}{L_{12}L_{13}}\right) \\ &\left. - 2d_1d_3m_3\cos\left(k\varphi_3\right)\left(\frac{1}{L_{13}^2}+\frac{1}{L_{12}L_{13}}\right) + 2m_2m_3d_2d_3\cos\{k(\varphi_2-\varphi_3)\}\left(\frac{1}{L_{12}L_{13}}\right)\right] \end{aligned} \tag{9}$$

$$\begin{aligned} i_{2,\rm rms}^2 = \frac{8V_1^2}{\pi^2\omega^2}\cdot\sum_{k=1}^{2m+1}\frac{1}{k^4}&\left[\left(m_2d_2\right)^2\left(\frac{1}{L_{12}^2}+\frac{1}{L_{23}^2}+\frac{2}{L_{12}L_{23}}\right)+\frac{d_1^2}{L_{12}^2}+\frac{\left(m_3d_3\right)^2}{L_{23}^2}\right. \\ &- 2d_1d_2m_2\cos\left(k\varphi_2\right)\left(\frac{1}{L_{12}^2}+\frac{1}{L_{12}L_{23}}\right) - 2m_2m_3d_2d_3\cos\left\{k\left(\varphi_2-\varphi_3\right)\right\}\left(\frac{1}{L_{23}^2}+\frac{1}{L_{12}L_{23}}\right) \\ &\left. + 2d_1d_3m_3\cos\left(k\varphi_3\right)\left(\frac{1}{L_{12}L_{23}}\right)\right] \end{aligned} \tag{10}$$

$$\begin{aligned} i_{3,\rm rms}^2 = \frac{8V_1^2}{\pi^2\omega^2}\cdot\sum_{k=1}^{2m+1}\frac{1}{k^4}&\left[\left(m_3d_{k3}\right)^2\left(\frac{1}{L_{13}^2}+\frac{1}{L_{23}^2}+\frac{2}{L_{13}L_{23}}\right)+\frac{d_1^2}{L_{13}^2}+\frac{\left(m_2d_{k2}\right)^2}{L_{23}^2}\right. \\ &- 2d_1d_3m_3\cos\left(k\varphi_3\right)\left(\frac{1}{L_{13}^2}+\frac{1}{L_{13}L_{23}}\right) - 2m_2m_3d_{k2}d_{k3}\cos\left\{k\left(\varphi_3-\varphi_2\right)\right\}\left(\frac{1}{L_{23}^2}+\frac{1}{L_{13}L_{23}}\right) \\ &\left. + 2d_{k1}d_{k2}m_2\cos\left(k\varphi_2\right)\left(\frac{1}{L_{13}L_{23}}\right)\right] \end{aligned} \tag{11}$$

TABLE I
COMPARISON BETWEEN CALCULATED AND SIMULATED i_1 RMS

Case	Control Variables (δ_1, δ_2, δ_3, φ_2, φ_3)	Considered Harmonic order (n)	Calculated $i_{1,rms}$ (A)		Error in theoritical Calculation (%)
			GHA Model Based	Simulation	
(a)	(0.8, 0.918, 0.656, 0.6256, 0.2569)	1	2.316	2.4901	6.992
		3	2.451		1.570
		7	2.477		0.526
		13	2.4823		0.313
(b)	(0.38, 0.212, 0.462, 0.397, 0.124)	1	1.7839	1.8278	2.402
		3	1.8152		0.689
		7	1.8213		0.356
		13	1.8261		0.093

Thus, the proposed GHA-model-based approach to quantify the port rms currents avoids the conventional complicated time-domain-analysis-based rms current calculation that involves complex computations, especially when the converter has multiple operating modes with a large number of control variables (φ_i, δ_j).

In the equivalent three-port converter network under study, power transfer through the line inductance is possible only between two distinct sinusoidal voltage sources that have the same frequency. Hence, applying the superposition theorem and approximating the power flow up to $(2m+1)$th harmonics, the power flow from port-a to port-b can be represented as follows:

$$P_{ab} = \frac{4}{\pi^3 f_{sw}} \cdot \sum_{k=1}^{2m+1} \frac{1}{k^3} \left[\frac{V_a V_b}{L_{ab}} d_{ka} d_{kb} \sin\{k(\varphi_b - \varphi_a)\} \right]. \tag{12}$$

Its magnitude depends on the corresponding phase difference $(\varphi_b - \varphi_a)$ of the respective port voltages, their duty cycles (d_{ka} and d_{kb}), terminal dc voltages (V_a and V_b), and the line inductance between the respective ports (L_{ab}), whereas the direction of the power flow is solely determined by the phase shift between the full-bridge cell voltages, i.e., $(\varphi_b - \varphi_a)$.

In this work, ports 2 and 3 are assumed as two output ports and the total normalized power sunk at ports 2 and 3 is expressed in (13) and (14), respectively

$$P_2 = P_{12} + P_{32} = \frac{8P_{\text{base}}}{\pi^2} \sum_{k=1}^{2m+1} \frac{1}{k^3} \left[\frac{3m_2 L_1}{L_{12}} d_{k1} d_{k2} \sin(k\varphi_2) + \frac{3m_2 m_3 L_1}{L_{23}} d_{k2} d_{k3} \sin\{k(\varphi_2 - \varphi_3)\} \right] \tag{13}$$

$$P_3 = P_{13} + P_{23} = \frac{8P_{\text{base}}}{\pi^2} \sum_{k=1}^{2m+1} \frac{1}{k^3} \left[\frac{3m_3 L_1}{L_{13}} d_{k1} d_{k3} \sin(k\varphi_3) + \frac{3m_2 m_3 L_1}{L_{23}} d_{k2} d_{k3} \sin\{k(\varphi_3 - \varphi_2)\} \right] \tag{14}$$

where $P_{\text{base}} = \frac{V_1^2}{2\pi f_{\text{sw}} L_1}$. In order to ensure desired load powers for some specific voltage levels at both the outputs, (13) and (14) can be solved for the control variables $\delta_1, \delta_2, \delta_3, \varphi_2$, and φ_3. Thus, although the power flow between the ports in a TAB is coupled in nature, by independently varying the phase shifts and the duty cycle control variables, power flow to the individual ports can be controlled separately.

It is observed that due to the cross-coupling of power flow between all the available ports, the total power sunk at each output port is not only dependent on that port's phase shift but also depends on the phase shift of the other output port. Hence, a rigorous study has been performed in this work to evaluate the dependence of the maximum transferrable output power to a particular port on the other port's load demand. For this purpose, the following assumptions are made to simplify the analysis.

1) *m* is considered to be 1 in (13) and (14).
2) All the line inductances in the Y-equivalent TAB circuit are considered to be same, i.e., $L_1 = L_2 = L_3$.
3) The duty cycles of the bridge voltages are 1, i.e., $\delta_1 = \delta_2 = \delta_3 = 0$.

Thus, the input and output port's powers can be given as follows:

$$P_1 = \frac{8P_{\text{base}}}{\pi^2} \left[m_2 \sin(\varphi_2) + m_3 \sin(\varphi_3) \right] \tag{15}$$

$$P_2 = \frac{8P_{\text{base}}}{\pi^2} \left[m_2 \sin(\varphi_2) + m_2 m_3 \sin(\varphi_2 - \varphi_3) \right] \tag{16}$$

$$P_3 = \frac{8P_{\text{base}}}{\pi^2} \left[m_3 \sin(\varphi_3) - m_2 m_3 \sin(\varphi_2 - \varphi_3) \right]. \tag{17}$$

The total sourced power given by (15) suggests that the maximum power that can be transferred to the individual output ports in a TAB is restricted by the voltage gains of the output ports besides the circuit line inductances, input dc voltage, and the operating frequency. As m_2 and m_3 increase, more power can be transferred to the outputs if other circuit conditions are kept the same. It can also be inferred from (16) and (17) that in order to maximize P_2 at the specific voltage gains, m_2 and m_3, φ_2 should be maximized while minimizing φ_3 between the range of 0–$\pi/2$. A clearer conclusion can be drawn when the power flows are studied at a specific operating point defined by $m_2 = m_3 = 1$. Now, to have a positive load power at port 3, the following condition should be met:

$$\varphi_3 > \varphi_2 - \varphi_3 \ or, \ \varphi_2 < 2\varphi_3. \tag{18}$$

The condition (18) limits the maximum possible value of φ_2. Thus, the maximum power that can be delivered to port-2 is restricted by the power demand by port-3 and the vice versa also holds true. A more accurate calculation of the maximum transferrable power to port-2 $(P_{2,\max})$ for a specific power demand at port-3 (P_3) and voltage gain conditions has been performed for the TAB converter under study (circuit parameters are given in Table II) using MATLAB and presented in Fig. 5 plots. The key takeaways from the plots under unidirectional power flow, i.e., both P_2 and $P_3 > 0$, are as follows:

1) as P_3 increases, $P_{2,\max}$ decreases while keeping m_2 and m_3 constant;
2) for a particular P_3 and m_3, $P_{2,\max}$ increases with increasing m_2;
3) $P_{2,\max}$ increases with the increase in m_3, while keeping P_3 and m_2 the same;
4) increasing both m_2 and m_3 for a particular P_3 will also increase $P_{2,\max}$.

TABLE II
TAB CIRCUIT PARAMETERS

Circuit Parameters	*Values*
Input DC voltage (V_1)	160V
Secondary Output Port Voltage (V_2)	100-140V, 120V(nominal)
Secondary Output Port Rated Power (P_2)	400W
Tertiary Output Port Voltage (V_3)	16-28V, 22V(nominal)
Tertiary Output Port Rated Power (P_3)	400W
Transformer Turns Ratio (N_1, N_2, N_3)	7:5:1
Magnetizing Inductance (L_m)	300μH
Total Leakage Inductances (L_1, L_2', L_3')	16μH, 15μH, 0.28 μH
Secondary side Output Capacitor (C_2)	86μF
Tertiary Output Capacitor (C_3)	47μF
Switching frequency (f_{sw})	100 kHz

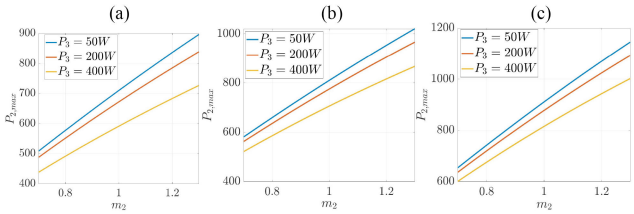

Fig. 5. Maximum transferable power to port-2 for different (m_2, m_3, P_3) conditions.

III. PWM TECHNIQUES IN TAB

As discussed in the previous section, the desired power flow in a dual-output TAB converter, given by (16) and (17), can be achieved by utilizing at least the two primary control variables: φ_2 and φ_3. Solving (16) and (17) for these two unknown variables while keeping the duty cycle variables $(\delta_1, \delta_2, \delta_3)$ at unity yields in singular solution $\{\varphi_2, \varphi_3\}$ for a particular voltage gain and load demand $\{m_2, m_3, P_2, P_3\}$ of the converter. Thus, only by controlling the phase shifts between the input and output full-bridge cells, the power transfer between the ports can be controlled, and this basic TAB PWM technique is known as DPS modulation. However, since this results in only one possible controller operating point, no loss optimization can be performed in such a two-variable control methodology. In order to get more flexibility in controlling the power flow in a TAB, one of the duty cycles $(\delta_1, \delta_2, \delta_3)$ of the bridge voltages is introduced as the control variables. More the duty cycle variables are taken into account to meet required load demand, the corresponding PWM strategy becomes more complex, and a bigger solution set of the control variables is generated. This also opens the possibility of TAB loss optimization by selecting the optimum control variables among the derived feasible solution set. Depending on the number of control degrees of freedom and their combinations, the PWM techniques of a TAB converter are broadly classified into eight categories as follows:

1) Dual Phase Shift (DPS): $\{\varphi_2, \varphi_3\}$;
2) Triple Phase Shift-1 (TPS-1): $\{\delta_1, \varphi_2, \varphi_3\}$;
3) Triple Phase Shift-2 (TPS-2): $\{\delta_2, \varphi_2, \varphi_3\}$;
4) Triple Phase Shift-3 (TPS-3): $\{\delta_3, \varphi_2, \varphi_3\}$;
5) Quad Phase Shift-1 (QPS-1): $\{\delta_2, \delta_3, \varphi_2, \varphi_3\}$;
6) Quad Phase Shift-2 (QPS-2): $\{\delta_1, \delta_3, \varphi_2, \varphi_3\}$;
7) Quad Phase Shift-3 (QPS-3): $\{\delta_1, \delta_2, \varphi_2, \varphi_3\}$;
8) Penta Phase Shift (PPS): $\{\delta_1, \delta_2, \delta_3, \varphi_2, \varphi_3\}$.

Among them, the simplest one is the DPS, whereas the PPS demands the highest computational complexity in return of maximum degrees of freedom. Thus, a calculated choice should be made while implementing any one of these to achieve an efficient power conversion throughout the wide output voltage gain and load range of the TAB while not overburdening the computational load of the digital implementation platform.

IV. MATHEMATICAL FORMULATION OF THE CONDUCTION LOSS OPTIMIZATION PROBLEM

In the quest to find the optimum controller operating point under the application of any PWM technique, a multivariable multiconstrained loss optimization problem is formulated in this article. Here, the objective function for minimization correlates with the total conduction loss that majorly contributes to the overall system loss in a TAB converter under light-load operation. The generalized objective function is formulated in (19), given as the sum of squares of the rms currents flowing in the TAB transformer windings, which is a suitable candidate for optimization because it is directly correlated with the conduction losses in the devices as well as the magnetic components of the converter

$$F(\delta_1, \delta_2, \delta_3, \varphi_2, \varphi_3, m_2, m_3) = (i_{1,\mathrm{RMS}}^2 + i_{2,\mathrm{RMS}}^{'2} + i_{3,\mathrm{RMS}}^{'2}) \tag{19}$$

where $\delta_1, \delta_2, \delta_3 \in [0, \pi/2]; \varphi_2, \varphi_3 \in [-\pi/2, \pi/2]; \; m_2, m_3 > 0$. The winding rms currents can be calculated from (9)–(11), which depends on the control variables and the output port voltage gains and load demands.

Now, to verify the usefulness of introducing the duty cycle control variables toward cost function minimization, the gradient of the objective function **F** is measured with respect to the duty cycle δ_1 and expressed as follows:

$$\nabla_{\delta_1} F = \frac{\partial F}{\partial \delta_1} = \frac{\partial i_{1,\mathrm{RMS}}^2}{\partial \delta_1} + \frac{\partial i_{2,\mathrm{RMS}}^2}{\partial \delta_1} + \frac{\partial i_{2,\mathrm{RMS}}^2}{\partial \delta_1}$$

$$= \frac{48V_1^2}{\pi^2 \omega^2 L^2} \cdot \sum_{k=1}^{2m+1} \frac{\sin(k\delta_1)}{k^3} \cdot$$

$$[m_2 \cos(k\delta_2) \cos(k\varphi_2) + m_3 \cos(k\delta_3) \cos(k\varphi_3) - 2\cos(k\delta_1)]. \tag{20}$$

Under the application of TPS-1 modulation, i.e., $\delta_2 = \delta_3 = 0$, the gradient expression from (20) reduces to (21)

$$\nabla_{\delta_1} F|_{\delta_2 = \delta_3 = 0} = \frac{48V_1^2}{\pi^2 \omega^2 L^2} \cdot \sum_{k=1}^{2m+1} \frac{\sin(k\delta_1)}{k^3} [m_2 \cos(k\varphi_2)$$

$$+ m_3 \cos(k\varphi_3) - 2\cos(k\delta_1)]. \tag{21}$$

For simplicity of the analysis, considering m = 1, ∇F_{δ_1} under TPS-1 operation is restructured as follows:

$$\nabla_{\delta_1} F|_{\delta_2 = \delta_3 = 0} = \frac{48V_1^2}{\pi^2 \omega^2 L^2} \cdot \sin(\delta_1) [m_2 \cos(\varphi_2)$$

$$+ m_3 \cos(\varphi_3) - 2\cos(\delta_1)]. \tag{22}$$

Now, checking the gradient value at $\delta_1 = 0^+$, we obtain the following: $2\cos(\delta_1) \approx 2 > m_2 \cos(\varphi_2) + m_3 \cos(\varphi_3)$ for any

φ_2 and φ_3 when m_2, m_2<1. Hence, for $m_2, m_2 \in [0, 1)$, a negative gradient, i.e., $\nabla_{\delta_1} F|_{\delta_1=0^+;\delta_2=\delta_3=0} < 0$ holds universally true. Thus, it can be inferred that instead of the basic DPS-based modulation, the application of TPS-1 modulation technique helps in reduction of the objective function for the mentioned operating space defined by (m_2, m_3, P_2, P_3). This also proves the drawbacks in the DPS-based modulation technique, which is unable to achieve the least sum of mean-square currents with only phase-shift-based control under a wide $\{m, P\}$ operating range.

Furthermore, in quest of validating the requirement of the higher order modulation techniques, such as QPS-3, over the TPS-1, we check the gradient of ∇F_{δ_1} with respect to δ_2 as follows:

$$\nabla_{\delta_2}(\nabla_{\delta_1} F) = \frac{48V_1^2}{\pi^2\omega^2 L^2} \cdot \sum_{k=1}^{2m+1} \frac{\sin(k\delta_1)}{k^2} \left[-m_2 \sin(k\delta_2)\cos(k\varphi_2)\right]. \tag{23}$$

Applying m = 1 in (23), it is found that

$$\nabla_{\delta_2}(\nabla_{\delta_1} F) = -\frac{48V_1^2}{\pi^2\omega^2 L^2} \cdot m_2 \sin(\delta_1)\sin(\delta_2)\cos(\varphi_2). \tag{24}$$

For $\delta_2 > 0^+, \nabla_{\delta_2}(\nabla_{\delta_1} F) < 0$ holds true at a specific $\delta_1(>0)$. Thus, at a given δ_1, QPS-3-based PWM will minimize **F** better than when TPS-1 is employed. Thus, it is proven that utilization of the higher order PWM strategy is beneficial in terms of minimizing the conduction loss but at the cost of increased computational burden.

Now, the conduction loss optimization problem in the TAB converter can be generalized for a five-variable control system defined by the PPS modulation logic, where the objective function $F(\delta_1, \delta_2, \delta_3, \varphi_2, \varphi_3, m_2, m_3)$ is minimized for a specific operating m_2, m_3 condition. The constraints in this problem are given by the power flow equations (25) and (26), which are modified versions of (13) and (14), derived earlier in the section

$$PE_1(\delta_1, \delta_2, \delta_3, \varphi_2, \varphi_3, m_2, m_3, P_2) = P_{12} + P_{32} - P_2 = 0 \tag{25}$$

$$PE_2(\delta_1, \delta_2, \delta_3, \varphi_2, \varphi_3, m_2, m_3, P_3) = P_{12} + P_{32} - P_3 = 0. \tag{26}$$

Thus, for a specific converter operating condition, defined by the output ports' voltage gain and load conditions (m_2, m_3, P_2, P_3), the multivariable, multiconstrained, and single-objective optimization problem can be stated as $\min F|_{m_2,m_3}(\delta_1, \delta_2, \delta_3, \varphi_2, \varphi_3)$ subject to $(a) PE_1|_{m_2,m_3,P_2}(\delta_1, \delta_2, \delta_3, \varphi_2, \varphi_3) = 0 (b) PE_2|_{m_2,m_3,P_3}(\delta_1, \delta_2, \delta_3, \varphi_2, \varphi_3) = 0$ for $\delta_1, \delta_2, \delta_3 \in [0, \frac{\pi}{2}]$ and $\varphi_2, \varphi_3 \in [-\frac{\pi}{2}, \frac{\pi}{2}]$. Solving this problem generates the optimal control variable set $(\delta_1^*, \delta_2^*, \delta_3^*, \varphi_2^*, \varphi_3^*)_{\text{opt}}$ that leads to the least conduction loss for a particular (m_2, m_3, P_2, P_3) set. The optimal variable synthesis approach is depicted through gradient descent algorithm presented in Section VI.

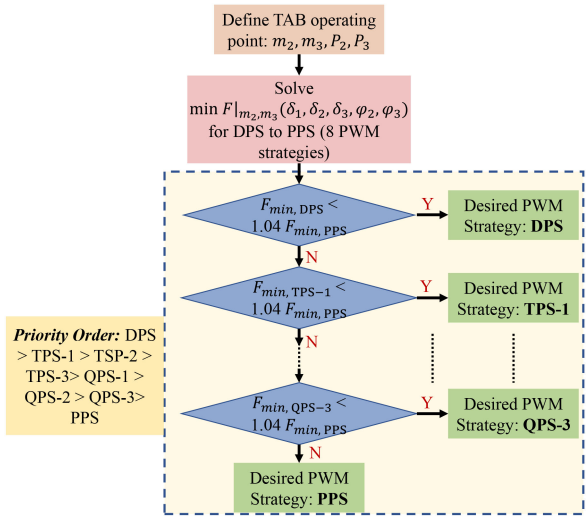

Fig. 6. Flowchart to achieve the optimum PWM strategy for any operating condition in a TAB.

V. Multivariable Optimization of Mean-Square Current and the Proposed Composite PWM Strategy

As the conduction loss optimization problem becomes well defined, it also indicates that engagement of five-variable control, i.e., the PPS modulation technique, will always provide the optimal conduction loss in a TAB control architecture. Nevertheless, implementing a PPS control across the whole output voltage gain and load range imposes a challenge to the TAB controller in terms of computationally expensive and large-memory lookup tables [7]. Therefore, a thorough effort is made in this work to identify the optimized and favorable PWM control strategy corresponding to the port voltage gain and power levels (m_2, m_3, P_2, P_3). Fig. 6 depicts the algorithm on how the optimum PWM strategy is identified for a particular operating condition. The fundamental notion behind the optimal modulation technique search is to employ a PWM technique that involves the least control degrees of freedom, i.e., lowest computational complexity, while attaining an $F|_{m_2,m_3}$ within 1.04 times of $F|_{m_2,m_3}$ under PPS-based modulation. Under this condition, we have searched the optimal PWM technique for a wide variation in m_2, m_3, P_2, and P_3 and presented it in Fig. 7. Here, the data are presented for a wide m_2 and P_2 variation (m_2 : from 0.7 to 1.3 and P_2 : from 50 to 400 W) under nine combinations of m_3 and P_3, owing to low, unity, and high gain ($m_3 = 0.8, 1$, and 1.2) and light, mid, and high load ($P_3 = 50$, 200, and 400 W) at port-3. The percentage reduction in computed objective function F under the influence of the optimal PWM strategy compared with the basic DPS modulation is also presented in the form of a contour plot. This helps visualize the benefit of optimized PWM technique for a particular operating zone over the conventional DPS-based control. The major takeaways from this plot are the following.

1) The basic DPS PWM strategy becomes the optimal technique for a broader (m_2, P_2) range as the output power increases from mid- to full-load at a particular port-3 voltage gain.

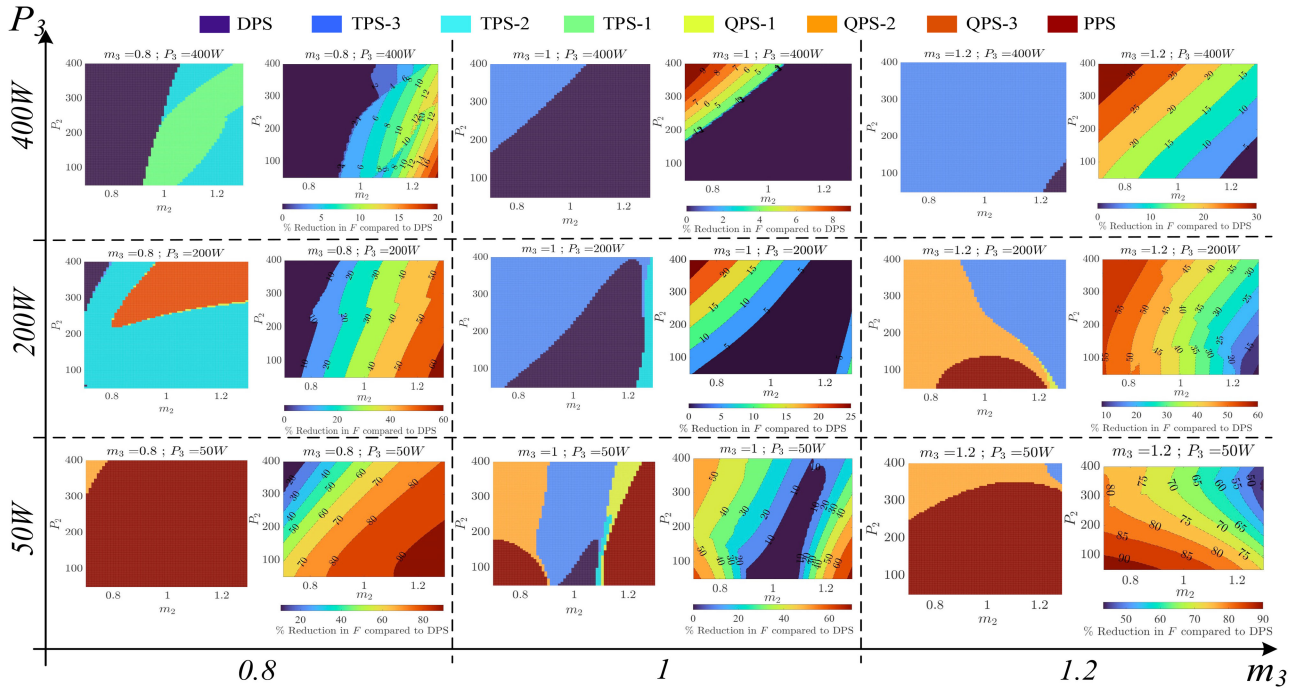

Fig. 7. Applicability of the PWM strategies in controlling TAB depending on the power and voltage levels.

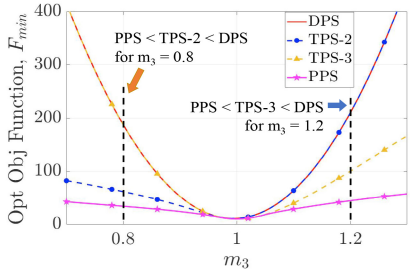

Fig. 8. Optimum PWM technique for a wide variation in m_3, for (P_3, m_2, P_2) = (50 W, 1, 174 W).

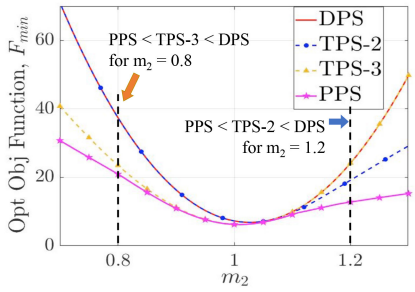

Fig. 9. Optimum PWM technique for a wide variation in m_2, for (P_2, m_3, P_3) = (200 W, 1, 18 W).

2) As the m_3 drifts away from unity, involvement of one order higher PWM technique, i.e., TPS, becomes necessary while maintaining high load at port-3.
3) Also, at $m_3 = 1$ as P_3 decreases, TPS, QPS, and PPS depending on the (m_2, P_2) condition turn out to be optimum candidates to maintain reduced conduction loss.
4) For light load at port-3, i.e., $P_3 = 50$ W, the utilization of the PPS becomes increasingly critical with the shift in $m_3$gain.
5) The composite as well as optimized PWM control technique becomes more beneficial as the converter approaches lighter load and nonunity gain operation at any of the output ports.

Fig. 8 depicts the variation in $F_{\min}$, achieved by different PWM strategies under a wide-gain and light-load (50 W) operation at port-3 for an operating condition of $(m_2, P_2) = (1,$ 174 W). Similarly, Fig. 9 shows the variation in $F_{\min}$, achieved by different PWM strategies under wide-gain and medium-load (200 W) operation at port-3 for an operating condition of $(m_3, P_3) = (1,$ 18 W). It is clear from Figs. 8 and 9 that at nonunity voltage gain conditions, the application of PPS becomes necessary to optimize the conduction loss in the TAB system.

The RMS currents through the transformer windings for varied load and voltage gain levels under the application of different modulations strategies are shown in Fig. 10. It can be observed that the proposed PWM scheme substantially reduces the bridge current RMS, specifically at light load and non-unity gain conditions.

VI. Implementation of the Optimized Switching Modulation Strategy in the TAB Converter

Upon the identification of the favorable as well as optimized PWM strategy for the TAB for specific port voltages and power levels, the optimum control variables are to be attained through an algorithm, realizable in the TAB controller. As mentioned in Section III, in the DPS PWM strategy, two degrees of freedom, i.e., $\varphi_2$and φ_3, are the only available system control variables. For any dual-output multiple-voltage electrical systems, two port currents of the converter, i.e., I_2' and I_3', and the output battery voltages, V_2' and V_3', are the control objectives. Such

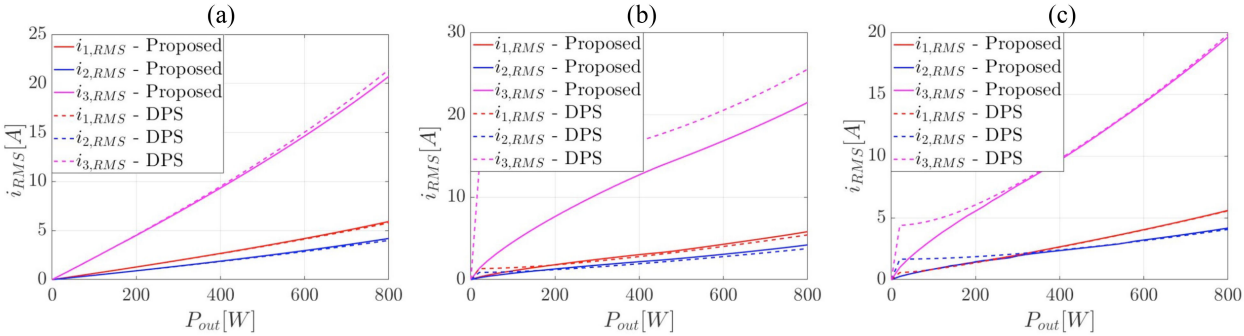

Fig. 10. Variation in the TAB transformer winding rms currents with increasing total output power (P_{out}) under only phase-shift-based DPS control and the proposed optimized control strategy for different output port voltage gains: (a) $m_2 = 1$ and $m_3 = 1$; (b) $m_2 = 1$ and $m_3 = 1.2$; and (c) $m_2 = 1.2$ and $m_3 = 1$.

a two-input ($\varphi_2$and φ_3) and multiple-output (I_2', I_3', V_2', and V_3') control system can be realized through three control loops, including two inner current loops and one outer voltage loop with decoupled power flow management, as presented in [7]. However, for higher order PWM strategies with inclusion of the duty cycle variables (δ_1, δ_2, and δ_3) in the control system, hardware implementation is only possible through the lookup-table-based approach in the existing literature. A TAB with the optimized conduction loss target will need a specific optimal control variable set for any operating point defined by the voltage gain and load conditions $\{m_2, m_3, P_2, P_3\}$ of the respective output ports. Generating a lookup table comprising of the duty cycle variables for each of the operating conditions will need multiple three-dimensional (3-D) arrays or 4D arrays to be computed first and then implemented in the DSP. This involves an extensive computational effort and requires a large memory in the controller. Moreover, the formulation of the lookup table while incorporating such an implementation strategy solely depends on the estimated or measured circuit parameters of the lossless TAB model, such as leakage/line and magnetizing inductances. In hardware, these values change according to the load variation and aging effects, and estimating them accurately is a challenging task. As a result, often during practical implementation, these precalculated optimum control values do not lead to the least conduction loss operation.

To avoid this drawback, in this article, we propose a model-independent gradient descent search algorithm to be implemented in the TAB controller to achieve the accurate optimal operating point. The gradient descent algorithm is primarily chosen for this multivariable, single-objective optimization problem due to its computational efficiency that produces a stable error gradient and a stable convergence [28]. Also, the variable learning rate provides flexibility to the designer while choosing between the execution time and the optimization accuracy of the algorithm. This proposed algorithm is shown in the form of a flowchart in Fig. 11. The algorithm starts with defining the steady-state operating system parameters, voltage levels, and power demand. This is followed by the identification of the optimized PWM strategy according to the output load and voltage gain levels, as described in Section V. Upon doing this, the values of the required duty cycle variables under the chosen PWM strategy are initialized as a vector $\delta(n)$containing $[\delta_1(n), \delta_2(n), \delta_3(n)]$. At the same time, the primary control variables, i.e., the phase shifts $\varphi_2(n)$and

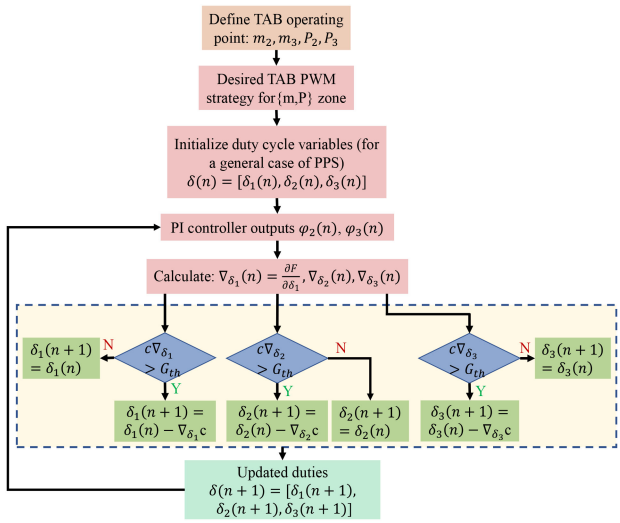

Fig. 11. Implemented algorithm to achieve the optimal control variables.

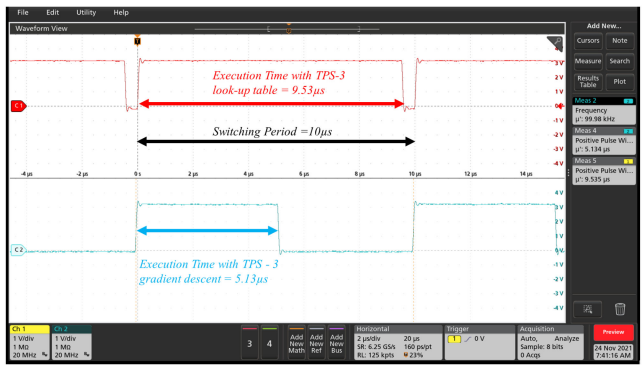

Fig. 12. Comparison between the control loop execution times of the lookup table and gradient-decent-search-based optimization approaches.

$\varphi_3(n)$, are adjusted by the implemented PI controller in order to meet the desired port voltage gains and the load demands, as shown in Fig. 1. Thus, the initial control variable set $[\delta(n), \varphi(n)]$ and the objective function $[F(n)]$ containing total rms current are deduced for a particular sample time (n). Now, in the next step, the gradient of F, ∇F, is measured separately for change in individual duty cycle variables. These gradients are expressed as $\nabla_{\delta_1}(n) = \frac{\partial F}{\partial \delta_1} = \frac{F(n+1)-F(n)}{\delta_1(n+1)-\delta_1(n)}$, $\nabla_{\delta_2}(n)$, and $\nabla_{\delta_3}(n)$. As long as these partial derivatives multiplied with the learning rate

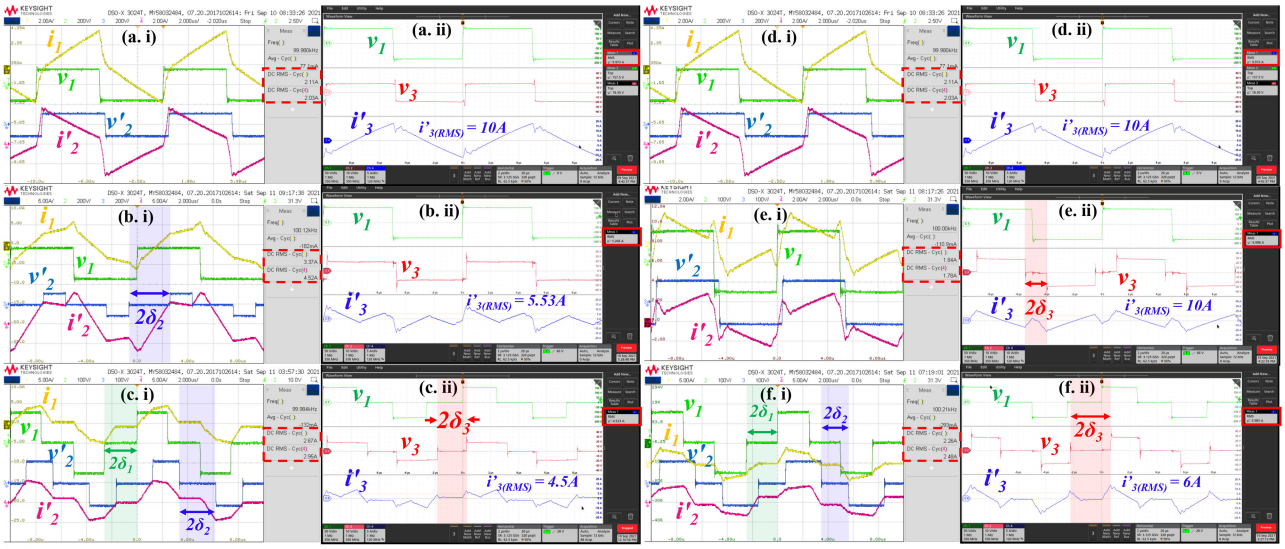

Fig. 13. Experimental TAB waveforms for (a)–(c) 160–114 V (174 W) and 18.3 V (50 W) conversion and (d)–(f) 160–114 V (174 W) and 27.4 V (50 W) conversion under the following PWM schemes: (a) DPS, (b) TPS-2, (c) PPS, (d) DPS, (e) TPS-3, and (f) PPS.

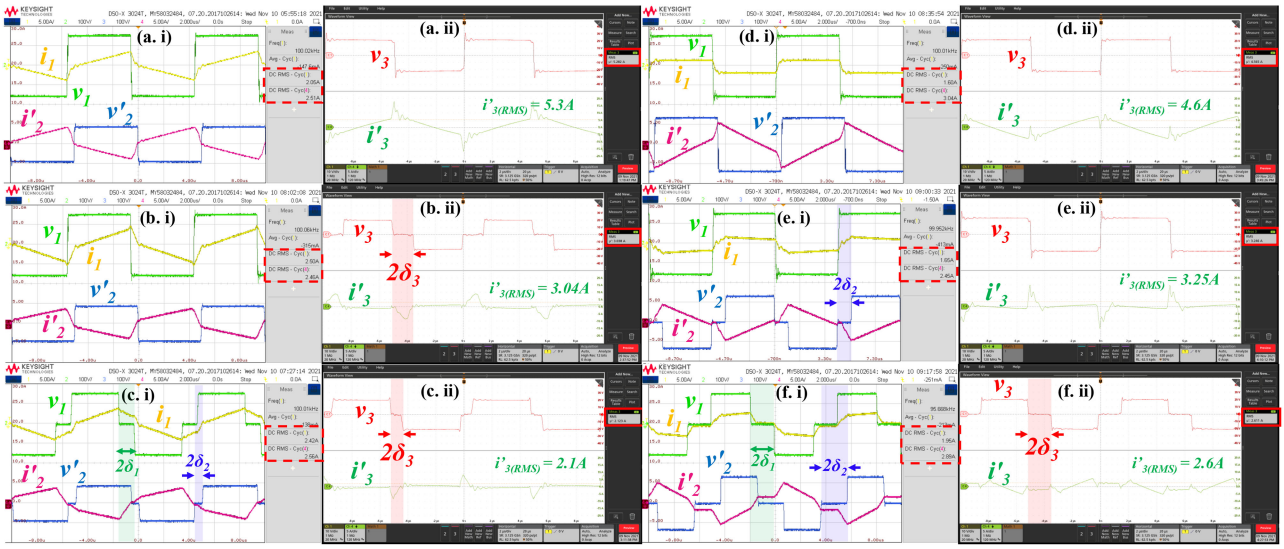

Fig. 14. Experimental TAB waveforms for (a)–(c) 160–91.5 V (200 W) and 22.8 V (18 W) conversion and (d)–(f) 160–138 V (200 W) and 22.8 V (18 W) conversion under the following PWM schemes: (a) DPS, (b) TPS-3, (c) PPS, (d) DPS, (e) TPS-2, and (f) PPS.

factor, **c**, are greater than the threshold $G_{\rm th}$, the search algorithm continues updating the duty cycle variables one at a time. At every iteration of this algorithm step, the phase-shift variables are also settled by the PI controller. Finally, the optimum duty cycles are obtained whenever $c\nabla_{\delta_1}, c\nabla_{\delta_1}, c\nabla_{\delta_1}$ become less than the threshold $G_{\rm th}$. The values of **c** and $G_{\rm th}$ are chosen based on the tradeoff between target accuracy in reaching the optimum operating point operation and the sensitivity and execution time of the algorithm. As the learning rate increases, the optimum point can be reached faster at the cost of increased system dynamics at the time of change in load and required voltage gain. Considering the continuous, dynamic, and generic nature of this algorithm, the approach can be implemented in any TAB converter.

To verify the usefulness of the proposed optimized control strategy, the execution time of the control logic is evaluated under different TAB operating conditions. Here, the execution time is selected as the ideal performance metric because it imposes an upper bound on the sampling frequency, i.e., the operating switching frequency of the converter. The results show that under the DPS, TPS, and PPS modes of operations, the execution times of the gradient descent algorithm are 4.05, 5.13, and 7.48 μs, respectively, which restricts the TAB switching frequency up to 247, 195, and 134 kHz, respectively. From these data, it can also be inferred that when a lower order control system is employed as the optimal control scheme, the TAB switching frequency can be increased considerably. Therefore, it facilitates the optimized variable frequency operation in a TAB architecture when the proposed control is utilized. Moreover, in order to compare the computational benefit of implementing this algorithm instead of the lookup tables in the DSP to optimize the

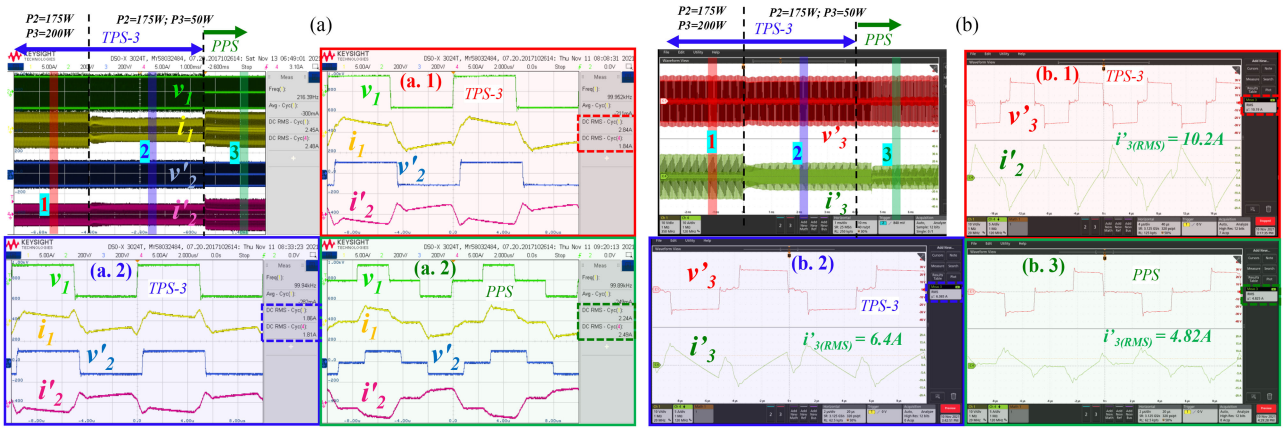

Fig. 15. Experimental TAB waveforms under load transient at port-3 (200–50 W) under 160–114 V (174 W) and 27.4 V conversion: (a) port-1 and port-2 circuit voltage and current waveforms; (b) port-3 voltage and current waveforms. Zoomed-in circuit waveforms before and after the load transient are shown in (a.1)–(a.3) and (b.1)–(b.3).

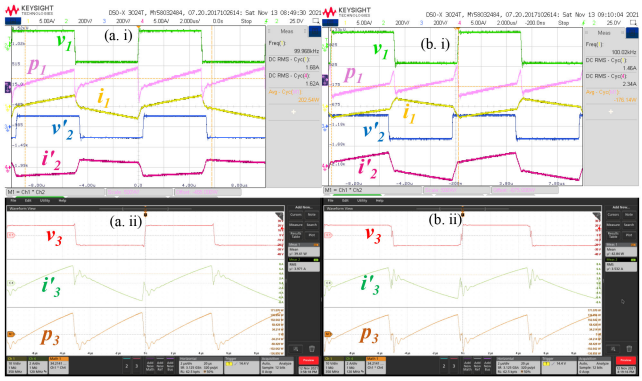

Fig. 16. Bidirectional operation of the TAB. (a) Power transfer from port-1 to port-2 and port-3. (b) Power transfer from port-2 to port-1 and port-3.

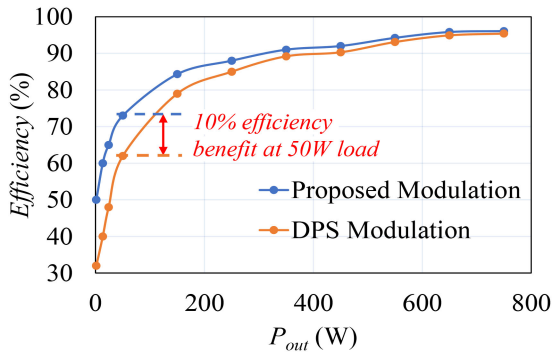

Fig. 17. Power loss distribution among the major power stage components of the TAB: semiconductor devices/switches and the transformer under the DPS, TPS, and the proposed optimal control strategy at different operating conditions defined by $\{m_2, m_3, P_2, P_3\}$ = (a) {1, 1.2, 400 W, 400 W}, (b) {1, 1.2, 175 W, 50 W}, and (c) {1.2, 1, 200 W, 18 W}.

power flow, a comparison is made between the two methods in terms of execution time in the same DSP. Observing Fig. 12, it is clearly noticed that the computational time of the lookup-table-based approach will be 1.86 times higher compared to the proposed gradient descent algorithm while implementing a TPS-3 modulation scheme in the TAB for a particular operating condition.

VII. Experimental Results and Discussions

Details of the proof-of-concept TAB dc–dc converter laboratory prototype and experimental results for verifying all the claims are presented in this section. The hardware setup of the fabricated 800-W TAB converter is specially designed for space shuttle applications. The salient parameters of the converter are given in Table II. The two full bridges of port-1 (input port) and port-2 (output port) are constructed in an identical manner, and each switch is realized by low $R_{\mathrm{DS(on)}}$ SiC MOSFET C3M0025065D (650 V, 25 mΩ, 97 A) manufactured by CREE. On the other hand, as the third port delivers high current at a low voltage level of 18—28 V, the corresponding full bridge is accomplished by employing GaN E-HEMT devices GS61008P (100 V, 8 mΩ, 90 A) from GaN Systems. The three full-bridge cells are coupled together through an integrated three-winding planar transformer that has a controllable leakage inductance feature. It is made of an E-shaped ferrite core "FR46410EC" and has a turns ratio of 7:5:1. The TAB control strategy is implemented using a single-core TMS320F28335 DSP and is placed in a separate control, interface and signal conditioning board. Results obtained with employing different PWM strategies in the TAB converter are presented below.

As seen in Section V, the engagement of the higher order PWM strategies become increasingly significant at lighter load and nonunity gain conditions. Thus, the application of the PWM strategies under two different light-load operating conditions is studied and presented in Fig. 13. It is noticed that the port-2 voltage gain (m_2) and power demand (P_2) are held at 1 and 174 W, whereas the port-3 voltage gain is changed in two steps (0.8 and 1.2), supplying a constant load of 50 W. The benefits of a higher order control system can be seen as prominent in Fig. 10(b), (c), (e), and (f), where the TAB is operated at $P_2 = 174\,\mathrm{W}, m_2 = 1, P_3 = 50\,\mathrm{W}$, (a)–(c) $m_3 = 0.8$, and (d)–(f) $m_3 = 1.2$, respectively, under (a), (d) DPS, (b) TPS-2, (e) TPS-3 and (c), (f) PPS PWM techniques. The key takeaways from these experimental results are as follows.

1) At under unity third-port voltage gain and light-load condition $(m_3 = 0.8)$, the TPS-2 control brings in an efficiency

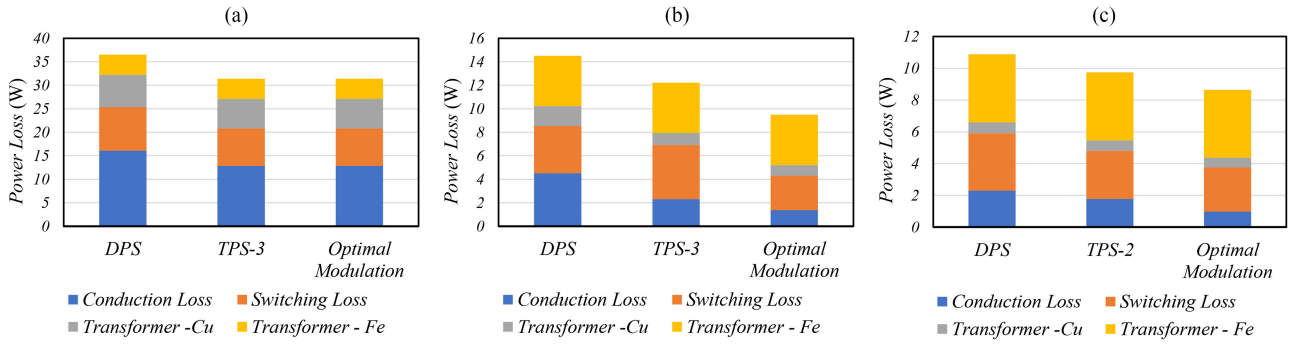

Fig. 18. TAB Efficiency versus output load comparison between conventional DPS and the proposed optimal control strategy under the output port voltage gain conditions of $m_2 = 1$ and $m_3 = 1.2$.

improvement with 47% reduction in i_3'. When PPS is used to optimize the power flow, the converter achieves an optimum total rms current condition incurring least loss. Here, PPS helps increasing the system efficiency by 1.8% by reducing **F** by 66% and hence minimizing the device conduction loss, winding loss and other Cu losses.

2) For over unity gain condition at light load in port-3 ($m_3 = 1.2, P_3 = 50\,\mathrm{W}$), only phase-shift control (DPS) results in high rms currents at the third winding ($i'_{3,\mathrm{RMS}} = 12.33\mathrm{A}$) with a peak current of ∼28 A, which incurs a higher conduction loss. Utilizing one order higher control scheme, TPS-2, the tertiary rms current is reduced by 19.1% with a 3% increase in the efficiency. However, the PPS, being the optimized PWM strategy for this operating zone, achieves an optimal efficiency of 87.1% at this light-load condition with 52% and 40% reduction in $i'_{3,\mathrm{RMS}}$, compared to DPS and TPS-2, respectively.
3) Under the operating conditions set by light load and nonunity gain at one port of the TAB, the PPS helps achieve the optimal operating point for most of the load and gain range of the other output port.

Fig. 14 presents the experimental waveforms of the TAB converter under wide-gain operation (changed in two steps: 0.8 and 1.2) at port-2 while keeping the port-3 at unity gain condition. It is noticed that the port-3 load demand (P_3) is kept as low as 18 W whereas port-2 is supplying a constant load of 200 W (P_2). The benefits of higher order control system can be seen as prominent in Fig. 11(b), (c), (e), and (f), where the TAB is operated at $P_2 = 200\,\mathrm{W}, m_3 = 1, P_3 = 18\,\mathrm{W}$, (a)–(c) $\mathrm{m_2} = 0.8$ and (d)–(f) $\mathrm{m_2} = 1.2$, respectively, under (a), (d) DPS, (b) TPS-3, (e) TPS-2, and (c), (f) PPS PWM techniques. The major highlights from these experimental results are the following.

1) At under unity second-port voltage gain condition ($\mathrm{m_2} = 0.8$), the optimal control scheme (PPS) brings in an efficiency improvement compared to the TPS-3 and DPS control schemes with a reduction in $\mathrm{i'_{3,RMS}}$ of 42% and 60.4%, respectively, and efficiency improvements of 1.4% and 0.9%, respectively.
2) For over unity gain condition in port-2 while keeping the other operating conditions same ($\mathrm{m_2} = 1.2, \mathrm{P_2} = 200\mathrm{W}, \mathrm{m_3} = 1, \mathrm{P_3} = 18\mathrm{W}$), the employment of PPS control brings the third winding current rms down to 2.6 A from 4.6 A and 3.25 A, under application of DPS and TPS-2, respectively. The optimized PPS PWM strategy improves the system efficiency by 1.2% compared to the DPS control under such an operating scenario.

Furthermore, in order to verify the capability of the implemented control algorithm to track the optimized PWM strategy operation under any output load or voltage variation, an experimental result is taken under a 75% load change at port-3. The waveforms presented in Fig. 15 indicate that TAB was operating under the TPS-3 modulation scheme before the load change, which is optimal at the operating point defined by $\{m_2, m_3, P_2, P_3\} = \{1, 1.2, 175\,\mathrm{W}, 200\,\mathrm{W}\}$. Following the load step-down event at port-3 ($P_3 = 50\mathrm{W}$), the converter still operates in the TPS-3 mode for 4.6 ms while dynamically searching for the optimized modulation scheme for conduction loss cost function minimization. After the search is over and the loss-minimized operating point is found, the converter transitions to the PPS mode of operation as it is the optimal modulation scheme for the operating condition defined by $\{m_2, m_3, P_2, P_3\} = \{1, 1.2, 175\,\mathrm{W}, 50\,\mathrm{W}\}$. Comparing third winding rms currents in Fig. 15(b.2) and (b.3), it can be validated that the proposed control strategy facilitates the online dynamic tracking of the optimized mean-square current and hence minimizes conduction loss in a TAB. Also, the output voltages are regulated at the same level by the PI controller under such a load transient event.

Fig. 16 represents the optimal DPS-modulation-based bidirectional power flow capability of the TAB dc–dc converter topology. In Fig. 16(a), port-1 is modeled as the input port while the other two ports are working as the loads, whereas in Fig. 16(b), port-2 is working as a source while the other two ports are the loads to the system. The power flow direction can be checked through an average of the instantaneous power waveform.

To showcase the benefits of loss optimization in the individual power stage components of the TAB converter, a power loss distribution analysis for the active switching network is also carried out and graphically presented in Fig. 17. The loss distribution among the semiconductor devices/switches and the transformer is studied under the DPS, TPS, and the proposed optimal control

strategy at different operating conditions defined by $\{m_2, m_3, P_2, P_3\}$ = (a) {1, 1.2, 400 W, 400 W}, (b) {1, 1.2, 175 W, 50 W}, and (c) {1.2, 1, 200 W, 18 W}. It is evident from the presented data that at light-load and nonunity gain conditions, the overall system conduction and switching loss is reduced by a substantial margin of up to 35% with the application of the proposed optimal PWM scheme. It can also be inferred from Fig. 17 that besides conduction loss, the proposed multivariable higher order switching modulation technique reduces the switching loss as well, under any nonunity TAB port voltage gain condition. This primarily occurs due to reduction in peak winding currents in the process of true rms value reduction.

The efficiency of the developed TAB converter is experimentally evaluated under the proposed modulation technique and the conventional DPS control for a wide sweep in output load while keeping the port-2 and port-3 voltage gain at 1.2 and 1, respectively. The efficiency plot, presented in Fig. 18, depicts that the proposed PWM technique brings an efficiency benefit of 10% at a light-load condition of 50 W.

VIII. Conclusion

This article presents an extensive analysis of multivariable PWM control in minimization of the sum of mean-square currents followed by experimental verification for the TAB dc–dc converter. The theoretical modeling of the TAB network is performed using the proposed frequency-domain GHA technique. It is mathematically proven that application of the duty cycle control along with the phase shift control optimizes the system conduction losses by providing higher degrees of freedom to the control system, especially at lighter load and nonunity gain condition. Application of the PPS control, which utilizes all five degrees of freedom, improves the light-load efficiency and reduces the designed transformer size by minimizing the winding current peaks and RMSs for wide gain power conversions. Hence, a composite and optimized PWM scheme that depends on load as well as input to output voltage ratio is proposed to leverage the advantages of all possible PWM control strategies while optimizing the system loss as well as control execution time. The composite PWM scheme experiences a seamless transition from DPS control at high load to TPS control at light load, and to PPS control as the voltage gain shifts from unity. The optimal control variable set for any of the PWM strategies is deduced using a gradient descent search algorithm that is implemented on a digital control platform. Experimental results indicate that the average sum of mean-square currents across the gain range from 0.8 to 1.2 at 30% load is reduced from 92.5 A^2 with DPS PWM to 59.37 A^2 with only TPS PWM, and finally to 31.27 A^2 with the proposed composite PWM strategy, leading to an efficiency improvement by 1.1% and 2.1%, respectively.

References

[1] A. K. Bhattacharjee, N. Kutkut, and I. Batarseh, "Review of multiport converters for solar and energy storage integration," *IEEE Trans. Power Electron.*, vol. 34, no. 2, pp. 1431–1445, Feb. 2019.

[2] S. Y. Kim, H. Song, and K. Nam, "Idling port isolation control of three-port bidirectional converter for EVS," *IEEE Trans. Power Electron.*, vol. 27, no. 5, pp. 2495–2506, May 2012.

[3] P. Wheeler and S. Bozhko, "The more electric aircraft: Technology and challenges," *IEEE Electrific. Mag.*, vol. 2, no. 4, pp. 6–12, Dec. 2014.

[4] C. Zhao and J. W. Kolar, "A novel three-phase three-port ups employing a single high-frequency isolation transformer," in *Proc. IEEE 35th Annu. Power Electron. Specialists Conf.*, 2004, vol. 6, pp. 4135–4141.

[5] A. Chandwani, A. Mallik, and A. M. Kannan, "A novel decoupled control scheme for phase controlled triple active bridge," in *Proc. 47th Annu. Conf. IEEE Ind. Electron. Soc.*, 2021, pp. 1–6, doi: 10.1109/IECON48115.2021.9589518.

[6] A. K. Jain and R. Ayyanar, "PWM control of dual active bridge: Comprehensive analysis and experimental verification," *IEEE Trans. Power Electron.*, vol. 26, no. 4, pp. 1215–1227, Apr. 2011, doi: 10.1109/TPEL.2010.2070519.

[7] D. Das and K. Basu, "Optimal design of a dual-active-bridge DC–DC converter," *IEEE Trans. Ind. Electron.*, vol. 68, no. 12, pp. 12034–12045, Dec. 2021, doi: 10.1109/TIE.2020.3044781.

[8] C. Zhao, S. D. Round, and J. W. Kolar, "An isolated three-port bidirectional DC–DC converter with decoupled power flow management," *IEEE Trans. Power Electron.*, vol. 23, no. 5, pp. 2443–2453, Sep. 2008, doi: 10.1109/TPEL.2008.2002056.

[9] S. Pistollato, N. Zanatta, T. Caldognetto, and P. Mattavelli, "A low complexity algorithm for efficiency optimization of dual active bridge converters," *IEEE Open J. Power Electron.*, vol. 2, pp. 18–32, Jan. 2021, doi: 10.1109/OJPEL.2021.3053058.

[10] W. Han, R. Ma, Q. Liu, and L. Corradini, "A conduction losses optimization strategy for DAB converters in wide voltage range," in *Proc. 42nd Annu. Conf. IEEE Ind. Electron. Soc.*, 2016, pp. 2445–2451, doi: 10.1109/IECON.2016.7793784.

[11] Y. Jiang, F. Liu, X. Ruan, and L. Wang, "Optimal idling control strategy for three-port full-bridge converter," in *Proc. Int. Power Electron. Conf.*, 2014, pp. 458–464, doi: 10.1109/IPEC.2014.6869623.

[12] Y. Tang *et al.*, "Reinforcement learning based efficiency optimization scheme for the DAB DC–DC converter with triple-phase-shift modulation," *IEEE Trans. Ind. Electron.*, vol. 68, no. 8, pp. 7350–7361, Aug. 2021, doi: 10.1109/TIE.2020.3007113.

[13] F. Wu, F. Feng, and H. B. Gooi, "Cooperative triple-phase-shift control for isolated DAB DC–DC converter to improve current characteristics," *IEEE Trans. Ind. Electron.*, vol. 66, no. 9, pp. 7022–7031, Sep. 2019, doi: 10.1109/TIE.2018.2877115.

[14] P. Purgat, S. Bandyopadhyay, Z. Qin, and P. Bauer, "Zero voltage switching criteria of triple active bridge converter," *IEEE Trans. Power Electron.*, vol. 36, no. 5, pp. 5425–5439, May 2021, doi: 10.1109/TPEL.2020.3027785.

[15] A. A. Ibrahim, T. Caldognetto, and P. Mattavelli, "Conduction loss reduction of isolated bidirectional DC–DC triple active bridge," in *Proc. IEEE 4th Int. Conf. DC Microgrids*, 2021, pp. 1–8, doi: 10.1109/ICDCM50975.2021.9504652.

[16] Y. Jiang, F. Liu, X. Ruan, and L. Wang, "Optimal idling control strategy for three-port full-bridge converter," in *Proc. Int. Power Electron. Conf.*, 2014, pp. 458–464, doi: 10.1109/IPEC.2014.6869623.

[17] R. Chattopadhyay, G. Gohil, S. Acharya, V. Nair, and S. Bhattacharya, "Efficiency improvement of three port high frequency transformer isolated triple active bridge converter," in *Proc. IEEE Appl. Power Electron. Conf. Expo.*, 2018, pp. 1807–1814, doi: 10.1109/APEC.2018.8341262.

[18] C. Fischer, S. Mariéthoz, and M. Morari, "An optimal modulation strategy for minimising the losses of isolated multisource DC–DC converters," in *Proc. 38th Annu. Conf. IEEE Ind. Electron. Soc.*, 2012, pp. 2174–2179, doi: 10.1109/IECON.2012.6388792.

[19] C. Fischer, S. Mariéthoz, and M. Morari, "Minimising conversion losses in isolated multisource DC–DC converters with non-negligible resistive components," in *Proc. IEEE Energy Convers. Congr. Expo.*, 2015, pp. 1575–1581, doi: 10.1109/ECCE.2015.7309882.

[20] M. Phattanasak, R. Gavagsaz-Ghoachani, J. Martin, B. Nahid-Mobarakeh, S. Pierfederici, and B. Davat, "Comparison of two nonlinear control strategies for a hybrid source system using an isolated three-port bidirectional DC–DC converter," in *Proc. IEEE Veh. Power Propulsion Conf.*, 2011, pp. 1–6, doi: 10.1109/VPPC.2011.6043161.

[21] E. S. Oluwasogo and H. Cha, "Self-current sharing in dual-transformer-based triple-port active bridge DC–DC converter with reduced device count," *IEEE Trans. Power Electron.*, vol. 36, no. 5, pp. 5290–5301, May 2021, doi: 10.1109/TPEL.2020.3029829.

[22] L. Piris-Botalla, G. G. Oggier, A. M. Airabella, and G. O. García, "Analysis and evaluation of power switch losses for three-port bidirectional DC–DC converter," in *Proc. IEEE Int. Conf. Ind. Technol.*, 2012, pp. 950–955, doi: 10.1109/ICIT.2012.6210061.

[23] S. Zou, J. Lu, and A. Khaligh, "Modelling and control of a triple-active-bridge converter," *IET Power Electron.*, vol. 13, pp. 961–969, 2020.
[24] J. Böhler, F. Krismer, T. Sen, and J. W. Kolar, "Optimized modulation of a four-port isolated DC–DC converter formed by integration of three dual active bridge converter stages," in *Proc. IEEE Int. Telecommun. Energy Conf.*, 2018, pp. 1–8, doi: 10.1109/INTLEC.2018.8612312.
[25] M. Jafari, Z. Malekjamshidi, and J. Zhu, "Design, analysis and control of a magnetically-coupled multi-port multi-operation-mode residential micro-grid," in *Proc. 20th Int. Conf. Elect. Mach. Syst.*, 2017, pp. 1–6, doi: 10.1109/ICEMS.2017.8056449.
[26] S. Gong *et al.*, "Sliding mode control based decoupling scheme for quad-active bridge DC–DC converter," *IEEE J. Emerg. Sel. Topics Power Electron.*, to be published, doi: 10.1109/JESTPE.2021.3096228.
[27] "Battery selection practice for aerospace power systems," submitted by MSFC to NASA, Feb. 1999.
[28] P. A. Parrilo, "Sum of squares optimization in the analysis and synthesis of control systems," 2006. [Online]. Available: http://www.mit.edu/∼parrilo/pubs/talkfiles/Eckman.pdf

Saikat Dey (Student Member, IEEE) received the B.Tech. degree in electrical engineering from the Indian Institute of Engineering Science and Technology, Shibpur, Shibpur, India, in 2018. He is currently working toward the Ph.D. degree in systems engineering with the Arizona State University (ASU), Polytechnic Campus, Mesa, AZ, USA.

From 2018 to 2020, he was a Power Electronics Design Engineer with Tagore Technology, India Centre, where he developed some highly efficient and compact power electronic converter solutions with Tagore's GaN power products. His major research interests include the design, control, and optimization of power electronic converters, highly efficient and high-power density power converter solutions using wide-bandgap semiconductors.

Mr. Dey was the recipient of various awards and recognitions, including the University Graduate Fellowship (2021), the Outstanding Research Award (2021) at ASU, and the Best Bachelors' Thesis Award from the Indian National Academy of Engineering (2018).

Ayan Mallik (Member, IEEE) received the bachelor's degree (B.Tech.) from the Indian Institute of Technology (IIT), Kharagpur, Kharagpur, India, in 2014, and the M.S. and Ph.D. degrees from the University of Maryland, College Park, College Park, MD, USA, in 2018 and 2019, respectively, all in electrical engineering.

He joined Arizona State University as an Assistant Professor in August 2019. His research interests include the design, control and multiobjective optimization of power electronic converters, highly efficient and high-density power conversion solutions in the applications of more-electric aircraft, electric vehicles, renewables, wireless charging, and data centers. He has authored/coauthored/coinvented more than 45 peer-reviewed publications and 2 U.S. patents. He has worked on research, development, and testing of regulated transformer rectifier units for more-electric aircraft, integrated bidirectional onboard charger design for electric vehicles, high-density dc–dc conversion for data centers, and many other projects.

Dr. Mallik was the recipient of various awards and recognitions, including first place in Dean's Doctoral Dissertation Award competition at UMD (2019), ECE Distinguished Dissertation Award at UMD (2019), University of Maryland's (UMD) Invention of the Year award (2018), Jimmy H.C. Lin Invention Award (2018), and third place in Allegheny Region Cleantech University Prize Collegiate Competition (2017) sponsored by the U.S. Department of Energy, among many others.